

# Statistics of traveling ionospheric disturbances at high latitudes using a rapid-run Ionosonde

Samson T. Moges<sup>1\*</sup>, Ruslan O. Sherstyukov<sup>1</sup>, Alexander Kozlovsky<sup>1</sup>,  
Thomas Ulich<sup>1</sup>, and Mark Lester<sup>2</sup>

<sup>1</sup>Sodankylä Geophysical Observatory, University of Oulu, Sodankylä, Finland

<sup>2</sup>Department of Physics and Astronomy, University of Leicester, Leicester, UK

## Key Points:

- Deep neural networking approach has shown its great potential for ionosonde driven MSTID studies.
- Daytime (nighttime) MSTIDs result from lower (upper) atmospheric/ionospheric sources.
- Ionosonde-Meteor radar collocated measurements reveal excellent agreement to MSTIDs studies.

---

\*Tähteläntie 62, Sodankylä, Finland

Corresponding author: Samson T. Moges, [samson.moges@oulu.fi](mailto:samson.moges@oulu.fi)

## Abstract

The potential of deep learning for the investigation of medium scale traveling ionospheric disturbances (MSTIDs) has been exploited through the Sodankylä rapid-run ionosonde in this statistical study. The complementing observations of the Sodankylä ionosonde with those of the Sodankylä meteor radar reveals the diurnal and seasonal occurrence rate of high-latitude MSTIDs for the first time in the recent low solar activity period, 2018 - 2020. In our results, the daytime, nighttime and dusk MSTIDs are predominantly identified during winter, summer, and equinoctial months, respectively. The winter daytime higher (lower) occurrence rate is well correlated with the lower (higher) altitude of the height of the F2-layer peak (hmF2), and the low occurrence rate of the summer daytime is well correlated with the mesosphere-lower-thermosphere wind shear and higher gradient of temperature. Relatively high occurrence rate ( $> 0.4$ ) of summer nighttime MSTIDs has a general – but not one-to-one agreement – with post-noon to evening IU (eastward auroral current index) inferred ionospheric conductivity. Rather, we see a one-to-one relationship between the summer nighttime MSTIDs and zonal wind shear suggesting that the wind shear-induced electrodynamic processes could play significant roles for higher occurrence rate of MSTIDs. Furthermore, significant MSTIDs with  $\sim 0.4$  occurrence rate are so far revealed during spring and autumn transition periods. The enhanced nighttime MSTID amplitudes during the equinox are observed to be well correlated with IL index (westward auroral current indicator) suggesting that the particle precipitation during substorms could be the primary cause.

## 1 Introduction

Travelling ionospheric disturbances (TIDs) are plasma density fluctuations that propagate as waves through the ionosphere at a wide range of velocities and frequencies. Depending on the spatial and temporal scales, TIDs are classified as large-scale (LSTIDs), medium-scale (MSTIDs) and small-scale (SSTIDs) having corresponding periods 30 min - 3 hr, 15 - 60 min, and 2 - 5 min, respectively (Hunsucker, 1982).

An important triggering mechanism of TIDs is atmospheric gravity waves (AGWs), which originate in the lower atmosphere due to the interplay of gravity and buoyant force combined with the effects of inertia (e.g. Hocke et al., 1996). AGWs affect the ionospheric plasma through modifying the background flow of the neutral gas/air and transfer the energy into the ionosphere via collision (frictional heating) (Hunsucker, 1982; Hocke et al., 1996). Following a thoroughly established theoretical explanation by Hines (1960), when these waves are detected in the ionosphere, they are interpreted as traveling ionospheric disturbances.

Extensive statistical studies of MSTIDs were carried out at low latitudes (e.g. Cândido et al., 2008; Pimenta et al., 2008; MacDougall et al., 2009) and midlatitudes (e.g. see review paper by Hocke et al. (1996)) to reveal local and global causative mechanisms. It is therefore understood that MSTIDs can be excited due to lower atmospheric gravity waves (Oliver et al., 1997; Kotake et al., 2007; Miyoshi et al., 2018; Otsuka, 2021) and Perkins instability (Perkins, 1973; Kelley & Miller, 1997; Hamza, 1999; Tsunoda, 2008) during the day and nighttimes, respectively. However, it was established that the Perkins instability is not sufficiently strong enough so as to explain the observed nighttime MSTID behaviour (Kelley & Makela, 2001), rather it could be supported by the E-F ionospheric coupling through instabilities at E region to have the required effect (Kelley et al., 2003; Cosgrove & Tsunoda, 2004; Yokoyama et al., 2009). Shiokawa et al. (2013) reported however that Perkins instability could still play the same role for the generation of nighttime MSTIDs at high latitudes. However, Perkins instability contribution is expected to be so small due to larger magnetic field inclination angles at high latitudes unless it is supported by some other electrodynamic processes mentioned above.

At high latitudes the dominantly discussed mechanism to generate TIDs include auroral sources related to intensive electrojet currents (Chimonas & Hines, 1970; Francis, 1974) and particle precipitation (Kirchengast, 1997). AGWs excited out of these sources may arrive F region either directly from the E region or progress downwards through the mesosphere to the earth and reflected back from the earth and again propagate to the F region (Francis, 1974; Bristow et al., 1996). In addition, the forcing driven by oscillations of the neutral air/gas density from the lower atmosphere is also thought to be a potential source of MSTIDs. These variants of AGWs may reach the F region ionosphere directly if the driving force is large enough, although the exponential decrease of neutral density with altitude creates exponentially growing wave amplitude that lead to wave breaking near the mesopause in combination with high temperature lapse rate, and then launch a secondary wave that can arrive the F region. The latter seems a more plausible mechanism because the damping effect of wave-medium interaction during propagation will not allow the wave to propagate from the troposphere directly through to the F region. The wave breaking altitude might show slight variation corresponding to the mesopause altitude below  $\sim 86$  km/  $\sim 95$  - 100 km during summer/winter at high latitude (Xu et al., 2007). AGWs induced via auroral electrojet current perturbations which propagated obliquely downwards and reflected back from the Earth may also reproduce secondary waves if they breakdown at the MLT region.

TIDs at high latitudes can also be driven by variations of  $\mathbf{E} \times \mathbf{B}$  drift and particle precipitation emanating from several nonlinear coupling processes such as frictional heating (Kirchengast, 1997). These types of TIDs are however less wave-like than AGW attributed TIDs. On the other hand, there are pulselike features that might stem from blobs in high latitudes. Blobs can originate from the distortion of polar cap patches due to the impact of high speed anti-sunward convection  $\mathbf{E} \times \mathbf{B}$  drift (Crowley et al., 2000) and/or created due to local particle precipitation (Jin et al., 2016). In either cases the steep plasma density enhancements which correspond to blobs could be detected as irregular signatures using ground based instrumentations. It should be noted however that MSTIDs have clear periodicity, in distinction from the irregular blobs.

At high latitudes, MSTIDs were studied efficiently using SuperDARN HF radars (e.g. Samson et al., 1989; Bristow et al., 1996). The signatures of MSTIDs on oblique HF radio signals, which are backscattered from the ground, can be observed by SuperDARN due to periodic focusing and defocusing of the signals (Samson et al., 1989). However, in the case of vertically incident signals from the ionosonde, MSTIDs can be detected by their alternate increase and decrease of the critical frequencies sounded by the receiver. This means that when MSTIDs are passing over the region, the ionospheric density oscillates back and forth corresponding to the period of the MSTIDs. In the earlier work, Kozlovsky et al. (2013) used the rapid-run SGO ionosonde to monitor AGW-TID characteristics in several frequency bands namely small-scale (10 -15 min), medium-scale (15 - 30 min), medium-large scale (30 - 60 min), and large scale (60 - 120 min) GWs. In their investigation they used the virtual height of reflection corresponding to their selected frequency which is between the critical frequencies at E and F region.

Numerous statistical studies of MSTIDs have been carried out at high latitudes. However, their efficiency is subject to the facilities used. For example, GPS driven MSTID studies at high latitudes are difficult due to two possible reasons. First, at high latitudes, GPS satellites do not pass overhead, and therefore the signals typically reach receivers at low elevation angles, which leads to low observed amplitudes of MSTIDs. Another evident problem is related to the passage of the GPS signal through multiple low and high ionospheric density regions of MSTIDs. Since the MSTID wavefronts propagate from their source at a slant angle as seen e.g., in incoherent scatter radar data from the ground, the same GPS signal will traverse both the crest and the trough sides of MSTIDs along their line of sight which leads to smearing out of the real ionospheric density variations. On the other hand, MSTIDs studies using optical measurements such as all-sky cameras

are limited only to nighttime, and incoherent scatter radar observations are not always available due to their high operating power demand.

Therefore, until recently, at daytime, experimental studies with better temporal resolution and long-term analysis were limited to SuperDARN observations. In this work, we used the rapid-run ionosonde that allows us to study MSTIDs at all local times. We focused on studying the daily and seasonal behavior of MSTIDs (periods 25 - 100 minutes) at a fixed location during the recent low solar activity period (2018 - 2020) using the 1-minute F2-layer critical frequencies (foF2) from the rapid-run Sodankylä ionosonde with using artificial intelligence (AI). To the best of our knowledge, this is the first statistical study of MSTIDs using high resolution (1 minute) ionosonde data of foF2 at high latitudes. The ionosonde enables us to measure amplitude, horizontal period, and occurrence rate distributions at the same location.

## 2 Materials and Methods

### 2.1 Data and material description

The ionosonde of Sodankylä Geophysical Observatory (SGO) is located at Sodankylä, Northern Finland (67.4° N, 26.6° E) to the equator side of the nightside auroral oval. Vertical ionospheric soundings have been performed by SGO since 1957. In 2005, a new digital ionosonde was introduced, which, until April 2007, produced an ionogram every 10 minutes. After the beginning of the International Polar Year 2007/08, the ionosonde was switched to perform 1-minute soundings. This “IPY-mode” operation continues to the present day. The ionosonde is a frequency-modulated, continuous wave (FM CW) chirp sounder (0.5 to 16 MHz), which transmits signals vertically up using a 64-m rhombic antenna. The radio signal is reflected back from the height where the plasma frequency equals transmitter frequency. The reflected signal from the ionosphere is mixed with the identical signal, synthesized by the receiver, and a windowed fast Fourier transform (FFT) is applied to obtain ionograms. Readers are referred to Kozlovsky et al. (2013) and Enell et al. (2016) for detailed information about the SGO ionosonde. From those ionograms, 12 ionospheric parameters (listed in Enell et al. (2016)) are then manually scaled by a well-trained specialist (scaler). While today the Sodankylä ionosonde produces ionograms with 1-minute cadence (1440 ionograms/day), careful parameter scaling takes time allowing for half-hourly ionogram interpretation (full analysis every hour, frequencies only at half-hours). This time resolution is insufficient to investigate medium scale traveling ionospheric disturbances (MSTIDs) with typical 20-70 minute periods (Ding et al., 2011). Therefore, a deep learning approach was implemented to recognize traces in ionograms and scale the minute-by-minute values of F2 critical frequencies.

To investigate possible effects of the large scale atmospheric circulation, data of the neutral wind in the mesosphere – lower thermosphere region were obtained from the meteor radar (MR) operated by the Sodankylä Geophysical Observatory. The physical basis behind this facility is that meteoroids entering the Earth’s atmosphere form ionized trails at heights between 80 and 100 km, which are transported by the wind and reflect radio waves. The Sodankylä MR is a commercially produced SKiYMET all-sky interferometric radar with standardized software for data processing (Hocking et al., 2001). It consists of one antenna transmitting spherical VHF waves at 36.9 MHz and five antennas receiving reflections from the meteor trails. The MR observations of the position and radial velocity of several thousand trails per day are used to determine the zonal and meridional components of the neutral wind at ~3 km intervals from 82 to 98 km altitude with one-hour time resolution. Here, we have used the zonal wind data averaged over 10 days to eliminate semi-diurnal tides and ~5-day planetary waves.

In addition, to investigate the possible source and/or dependence of TIDs on auroral current systems, International Monitor for Auroral Geomagnetic Effects (IMAGE)

indices of geomagnetic activity (specifically, IU and IL indices) were used. The IU and IL indices are measures of total eastward and westward ionospheric currents, respectively (Tanskanen, 2009). The indices are computed from at most 40 magnetometer stations (spanning 51.4° - 78.92° N geographic latitude) located in/or in the vicinity of the Nordic countries. For the actual representation of auroral current without the solar quiet (Sq) current contribution, the quiet time baseline was determined in every 3 hours and the minimum average baseline among the stations was subtracted from the X-component (North-South) magnetic field component.

## 2.2 Deep learning

Convolutional neural networks (CNN) are at the core of most state-of-the-art computer vision solutions for a wide variety of tasks. The recognition accuracy of CNN highly depends on the depth of CNN (number of convolution layers) and the complexity of its architecture. Architectures of CNN made significant progress initially by increasing layers depth (AlexNet, VGG16, VGG19 architectures) (Simonyan & Zisserman, 2014; Krizhevsky et al., 2017) then through the improvement of computing resources, utilization with Inception modules (GoogleNet, InceptionV1, InceptionV2, InceptionV3 architectures of deep CNN) (Szegedy et al., 2016) and finally solving the degradation problem with residual blocks (ResNet18, ResNet34, ResNet50, ResNet101, ResNet152 architectures of deep CNN) (He et al., 2016). The dataset used for CNN training contains 86500 ionograms for 2010-2020 years with manually scaled parameters for each ionogram. Several architectures of deep CNN were tested (VGG19, InceptionV3, Resnet101) and the best results for this dataset were reached by InceptionV3 architecture. Classifying layers of types F1, F2, including the absence of either layer, as well as a regression task to define the critical frequency of the F2 layer was undertaken. The accuracy of classification in the validation dataset showed 93% of correct predictions (see confusion matrix on Figure 1). The accuracy of regression on the validation dataset showed a root mean square error (RMSE) equal to 0.16 MHz, and mean absolute error (MAE) equal to 0.09 MHz (see errors distribution in Figure 1).

## 2.3 Methods of analysis

In the present study, we use the data of foF2 obtained by the deep learning techniques applied to all ionograms collected during three years from 1 January 2018 through 31 December 2020. Data losses in the ionograms archive is not common, but the analyzed foF2 critical frequency data from ionograms possesses significant data gaps, mostly because of absorption, blanketing, or broadcast interference in which cases the F2 trace is not identified at the ionograms (mostly in winter night times).

Figure 2 shows an example of how data is processed for 15 December 2020. The blue line in the top panel shows one-minute foF2 data obtained by the deep learning procedure (predicted values) whereas red dots indicate the values obtained by the manual scaling. To infer MSTIDs, the data were band-pass filtered using the Butterworth three-order filter at 25 - 100 minutes, which corresponds to the MSTID period band. This approach essentially removes ionospheric irregular features such as auroral blobs that have non-periodic content. Before the filtering, we interpolate data gaps via “Nearest” basis. However, we removed corresponding data points from the data set after filtration. Then, only hours containing at least 40 data points (66.7%) are analyzed. An example of the analyzed filtered data is given in the lower panel whose brief description is labeled by the text under the plot. The hourly status of data availability is labeled as “Yes” if the condition of 40 data points is met and “No” otherwise. The same labeling is carried out for amplitude (values printed in third row) based TID identification except “-” are marked for hours that do not meet the required data, i.e 40 data points.

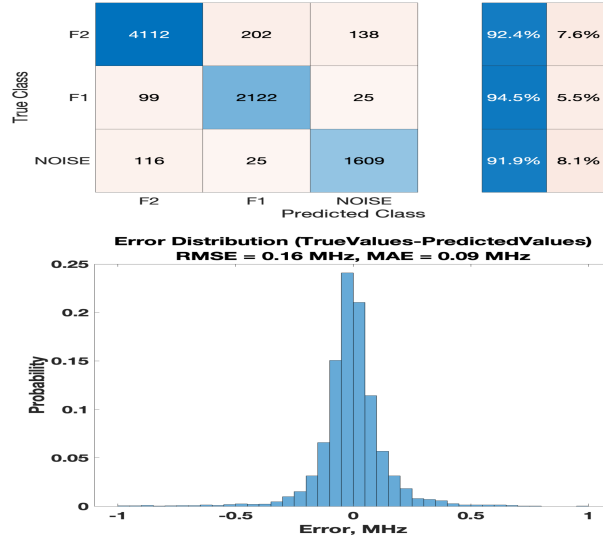


**Figure 1.** Original ionograms with 525x590 pixels were filtered and resized to a pixel sizes of 256x256 to save computing resources. InceptionV3 CNN architecture is then used to train 86500 manually scaled ionograms. Training has done based on optimization of CNN parameters with respect to minimization of the loss function. For classification task the cross entropy loss function  $L_{class}$  and for the regression task the mean square error (MSE) loss function  $L_{reg}$  were used. (Top panel) Confusion matrix to the classifier, and (bottom panel) error bars distribution with the root mean square error (RMSE = 0.16 MHz) and the mean absolute error (MAE = 0.09) for the regression task.

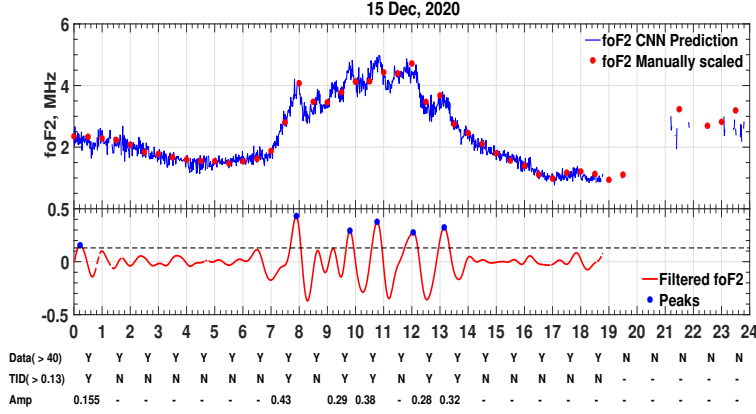


**Figure 2.** (Top panel) the foF2 data (hourly scaled (red dots) and its every minute prediction via deep learning (blue line)) for 15 December, 2020. (Bottom panel) maintained data after a band-pass butterworth filtering in a bandwidth of 25 - 100 minutes. (Bottom text) data matrix for the day considered, Y and N represent “Yes” and “No” for the request labeled to the left for each hour, and the hyphen line (“-”) indicates the absence of data.

The climatology plot of the data availability after removing data points that does not meet our requirement (containing less than 66.7% of data per hour) is shown in Figure 3. To identify MSTIDs using our method we needed to specify the minimum threshold frequency. This threshold is specified in order to compensate the algorithmic error of the method. Both classifications and regression analysis were carried out using a CNN InceptionV3 deep learning architecture. This yields a root mean square error (RMSE) and mean absolute error of 0.16 MHz and 0.09 MHz, respectively. Therefore, we chose the threshold frequency 0.13 MHz reasonably close to these algorithm inaccuracies.

The occurrence rate of MSTIDs was calculated on a monthly basis. We prepared a monthly-hourly bin for our MSTID cases. The calculation of the occurrence rate is given by:

$$Probability = \frac{X}{N} \quad (1)$$

where X is the number of MSTID cases detected in each hour and month, N is the number of unique hours in a month that have more than 40 data points.

### 3 Results

Multi-instrument observations by ionosonde, meteor radar and magnetometers were carried out to simultaneously observe ionospheric plasma perturbations, mesosphere neutral winds, mesosphere temperatures and local geomagnetic activity. We have plotted diurnal-seasonal distributions of MSTID occurrence rate, MSTID amplitude, MSTID period, mesosphere zonal neutral wind velocities and temperature, and local IU, IL indices for 2018-2020. This presentation allows us to classify TIDs by behavior patterns.



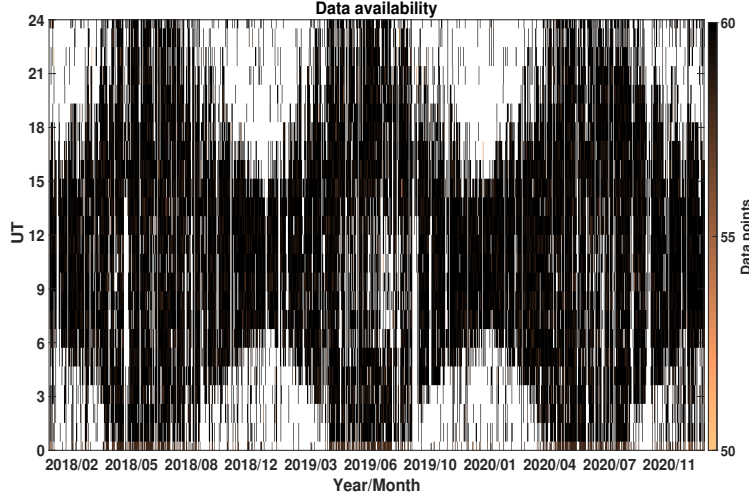


**Figure 3.** The climatology of predicted foF2 data availability between 2018 - 2020, (40 data points per hour is the minimum threshold and hours with less than 40 data points are shown as white portions in the plot).

### 3.1 Occurrence rates of TIDs

Figure 4a shows the universal time ( $LT=UT+2$ ) and seasonal variations of MSTID occurrence rate. The color bar indicates the probability of MSTID appearance in a certain month/hour bin. Black and white lines show average winter (December) and summer (July) hmF2 diurnal variations, respectively, calculated according to the IRI-2016 model. Figure 4a reveals three separate patterns of behaviour of MSTID occurrence which are (i) October - April, when the peak occurrence rate is during the daytime, (ii) June - October, when the peak occurrence rate is during the nighttime, and (iii) in April - June, and September - October, when there is a peak in occurrence rate near dusk. We discuss each of these in detail in turn.

From October to April the MSTID occurrence rate peaked at over 0.5 in the daytime, between 08:00 and 13:30 UT. Either side of this, between 02:00 and 07:00 UT, and between 15:00 and 18:00 UT the MSTID occurrence rate tends to zero. For the same months we observe nighttime MSTIDs from 18:00 to 01:00 UT with medium occurrence rate in range of 0.3-0.5. We have less confidence about MSTIDs occurrence rate for winter nighttime with respect to other time periods, due to the low data availability at this time (see Figure 4a).

The hmF2 diurnal variations have two strong maxima and minima (see the overlaid lines on Figure 4a). These hmF2 variations show a good agreement with the diurnal change of MSTID occurrence rate. Values of hmF2 less than 310 km coincide with the higher MSTID occurrence rate for time intervals from 08:00 to 13:30 UT. Values of hmF2 values greater than 310 km coincide with the lower MSTID occurrence rate for time intervals from 02:00 to 07:00 UT and from 15:00 to 18:00 UT. The MSTID occurrence rate and hmF2 from 18:00 to 01:00 UT have the same tendency, but MSTID occurrence rate at this time is lower than for daytime and, as mentioned previously, there is a lower confidence level due to the low data availability.

From June to September MSTID demonstrate the opposite behaviour to that from October to April. A high MSTID occurrence rate of more than 0.4 is observed in the nighttime between 21:00 and 01:00 UT. The MSTID occurrence rate is less than 0.3 between



01:00 and 15:00 UT. The time interval between 15:00 and 21:00 UT seems to be a transition period between day and night with an occurrence rate around 0.4.

The hmF2 diurnal variations again show agreement with the diurnal change of MSTID occurrence rate, but this correlation from June to September is opposite to that observed for Winter and Autumn. Values of hmF2 greater than 290 km correspond to the higher MSTID occurrence rate for time intervals from 21:00 to 01:00 UT. Values of hmF2 less than 280 km coincide with the lower MSTID occurrence rate for time intervals from 01:00 to 18:00 UT.

From April to June (spring) the MSTID occurrence rate increases up to 0.4 at dusk and lasts for approximately two hours. In Figure 4a this behaviour is seen as band of increased MSTIDs occurrence rate which tends to change appearance time from 13:00 UT in mid-April to 19:00 UT in mid-June (6 minutes/day, the onset (or occurrence) of MSTIDs changes with time at a rate of 6 minutes per day). The opposite shift of the MSTID appearance time from 19 to 13:00 UT is observed from September to mid-October (8 minutes/day).

We compare the annual variation of MSTID occurrence rate measured at the maximum height of F2 layer and neutral zonal wind velocities at heights between 82 - 98 km averaged over 3 years, 2018-2020 (see Figure 4a,b). From October to April (type 1) an eastward zonal wind dominates at these heights, and in April - mid-May the zonal wind reverses to westward. Between mid-May and mid-September, the zonal wind is strongly eastward above 88 km and westward below, such that a strong zonal wind shear occurs at this height which is a well-known phenomenon (e.g. Lukianova et al., 2018). The presence of the wind shear coincides with the extremely low MSTID occurrence rate during mid-May through mid-September. The westward wind in mid-April through mid-May fits the low MSTID occurrence rate as well. From October to April when eastward zonal wind is dominant the highest MSTID occurrence rate more than 0.5 is observed.

Annual variations of mesosphere temperature also agree with daytime MSTIDs occurrence rate. From April to mid-September mesosphere temperatures drop below 150 K, while daytime MSTIDs are observed with an occurrence rate of less than 0.3 (Figures 4a,b).

The IU index, Figure 4c stayed maximal from April to October similar to the occurrence rate of nighttime MSTIDs in summer. Nevertheless, the time of MSTIDs appearance and the enhanced IU index has spaced in time by 6 hours, approximately. However, the IU index indicates the geomagnetic activity due to eastward electrojet, which depends not only on the electric field but also on the ionospheric conductivity.

### 3.2 Amplitudes of TIDs

As briefly described in section 2 we calculated the MSTID amplitude from the filtered foF2 values above a threshold of 0.13 MHz. Figure 5a presents the diurnal-seasonal distribution of MSTID amplitude. The amplitude values during low MSTIDs occurrence rate (less than 0.15) were removed. The daytime MSTID amplitudes behaves in a similar fashion to the occurrence rate behaviour pattern. From mid-October to mid-March between 09 and 14:00 UT the amplitudes of the MSTIDs are close to 0.25 MHz. From mid-March to mid-October daytime amplitudes of MSTIDs are close to threshold 0.13 MHz. However, the opposite amplitude and occurrence rate behaviour is observed for nighttime TIDs on January and March and from mid-August to December. These TIDs are observed with amplitudes greater than 0.3. We note that winter nighttime TIDs amplitudes have a lower confidence level due to the low data availability.

The IL index is more sensitive to magnetosphere activity it increases at nighttime between 21 and 03:00 UT and more prominent during equinox months (see Figure 5b).

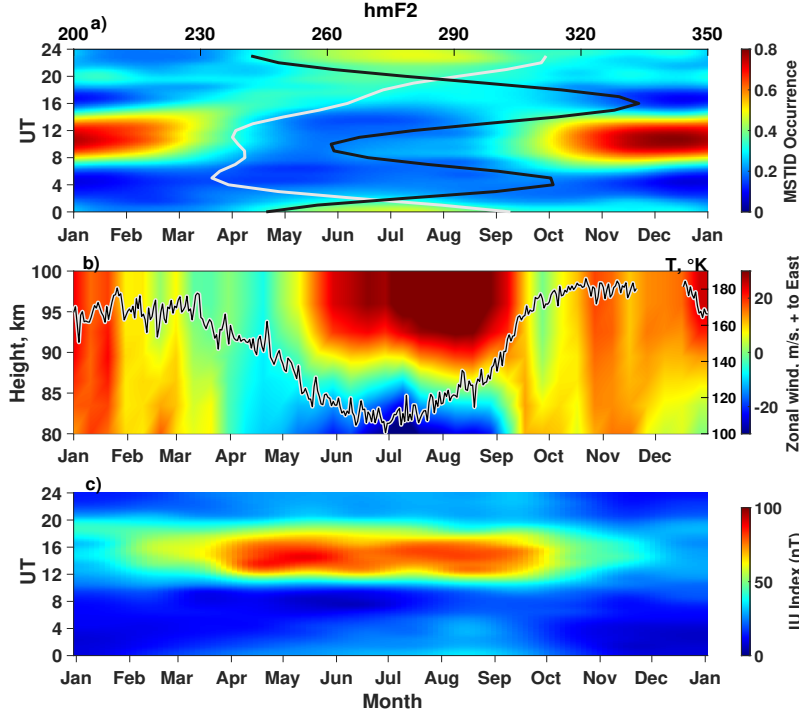


**Figure 4.** (a) The occurrence rate distribution of MSTID with IRI-2016 provided hmF2 (Top axis)) for Sodankylä during December (black solid line) and July (white solid line) are overlaid. Here we used the model hmF2 instead of our measurement because Sodankylä ionosonde is measuring h'F (the lowest virtual height of F layer) not the altitude of maximum ionisation, hmF2. (b) Zonal wind velocity pattern inferring the presence of strong wind-shear during the summer months with the mesospheric temperature (Right axis) overlaid (black line) from Sodankylä meteor radar, and (c) IU-index (IMAGE electrojet index (eastward)) obtained from International Monitor for Auroral Geomagnetic Effects (IMAGE) magnetometer networks over Scandinavia.

Thus, the IL index have a good agreement with nighttime TIDs amplitudes at least for equinox months with normal data availability.

### 3.3 Period of MSTIDs

A wavelet analysis was applied to determine the dominant period information of MSTIDs in the filtered data set. A continuous wavelet transform with Morlet wavelet function was used (Torrence & Compo, 1998). The Morlet wavelet function ( $\psi(x) = e^{-x^2/2} \cos 5x$ ), enabled us to obtain the dominant periods as a function of the scaled power in the time series domain. A wavelet with Continuous Wavelet Transform (CWT) has been found as an efficient method to detect the dominant wave parameters as observed by, for example, (Habarulema et al., 2013; Moges et al., 2022; Nigussie et al., 2022). We compute the periods of MSTIDs in each day and averaged for corresponding months as seen in Figure 6. The period seems to have a symmetrical distribution over seasons. More prominently, in winter months the MSTID periods are shifted to longer periods centered at about 60 minutes, while in summer both the maximum and the dominant modes of MSTID periods become shorter. It also shows lower period modes of MSTIDs are better accommodated in summer than in winter.

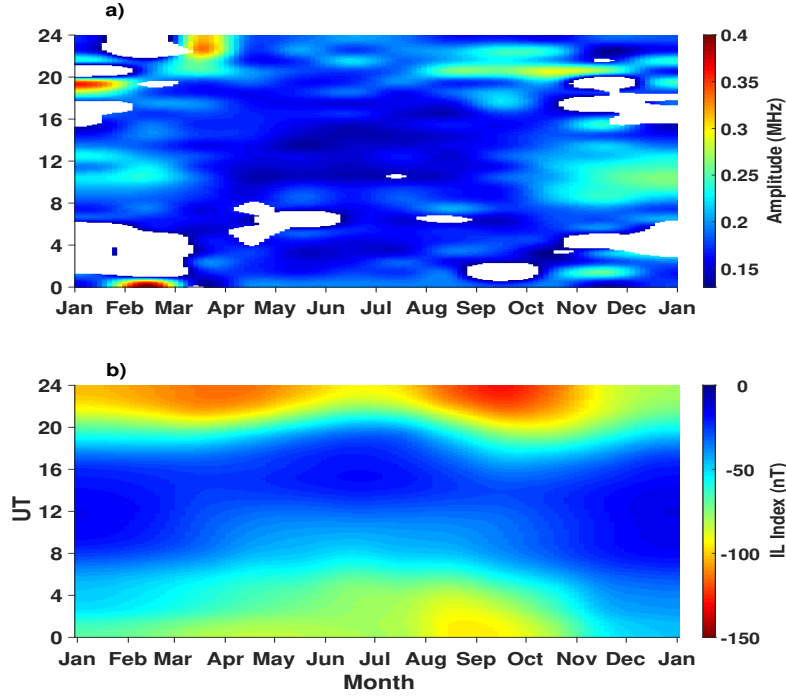


**Figure 5.** (a) Seasonal and diurnal distribution of TID amplitude above 0.13 MHz threshold. The amplitude distribution with low data availability and low occurrence rate (less than 15%) of TID is indicated in a white enclosure. (b) IL-index (IMAGE electrojet index (westward)) obtained from International Monitor for Auroral Geomagnetic Effects (IMAGE) magnetometer networks over Nordic.

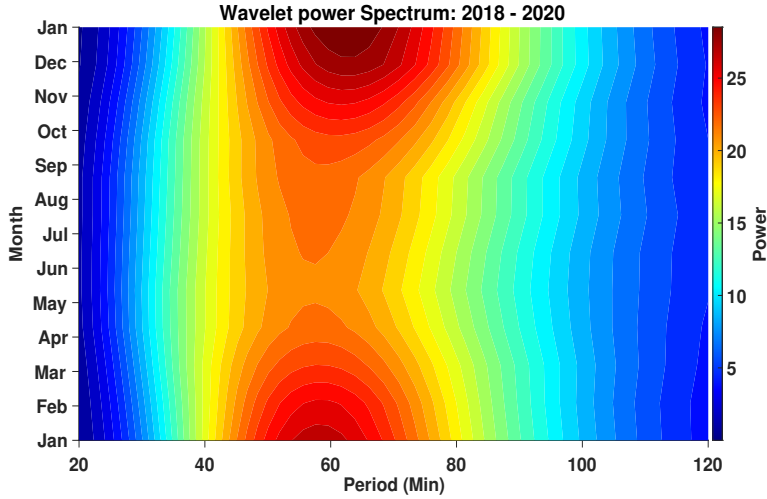


**Figure 6.** The monthly MSTID period-power spectrum distribution computed using morlet function by the Matlab code adapted from <http://paos.colorado.edu/research/wavelets/>.

## 4 Discussion

In this statistical study we have analyzed the occurrence probability of MSTIDs and their characteristics using the rapid-run SGO ionosonde during the recent solar minimum, in 2018-2020. Increased attention to MSTIDs is associated with the development of instruments and methods that make possible continuous observation of ionospheric parameters with high spatial and temporal resolution. The main goal of these studies was to define sources and mechanisms of MSTIDs generation. The most detailed vertical structures of MSTIDs were derived from Incoherent scatter radar data (Djuth et al., 2010), and their horizontal structures were inferred from optical instruments and GNSS receiver networks (Kubota et al., 2000; A. Saito et al., 2002; Tsugawa et al., 2007). However, most TID statistical studies at low, mid and high latitudes were made by GNSS methods of trans-ionospheric sounding due to the easily available data of total electron content (TEC) (Oluwadare et al., 2022; Ding et al., 2011; Afraimovich et al., 1999). Our study focuses on the diurnal and seasonal MSTIDs characteristics inferred from the foF2 ionosonde data, which were earlier used mostly to observe background ionospheric ionization. Sherstyukov et al. (2018) compared MSTID manifestation in TEC perturbation maps and ionograms and have shown that foF2 variations are a reliable way to observe MSTIDs propagating over ionosondes at hmF2 heights. Then, implementation of deep learning to obtain one-minute foF2 data allowed us to conduct this statistical study of MSTIDs.

Based on characteristics of the observed MSTIDs, Kotake et al. (2007) categorized MSTIDs in three types: daytime, nighttime, and dusk MSTIDs. In our study, we also clearly observe these three dominant patterns of the MSTIDs occurrence rate described above. Daytime MSTIDs most frequently occur in October - April, nighttime MSTIDs in June - October, and dusk MSTIDs in April - June and September - October. Using data from a collocated meteor radar, we have investigated the possible dependence of the observed MSTIDs on the neutral wind and temperature at 80-100 km.

### 4.1 Daytime MSTIDs

Numerous theoretical and experimental works considered AGWs as the main source of MSTIDs (Hines, 1960; Oliver et al., 1997; Kotake et al., 2007; Miyoshi et al., 2018; Otsuka, 2021). Most of the studies used two criteria to select MSTIDs caused by AGWs: the first is matching observed MSTIDs parameters with AGWs parameters according to dispersion relation (Medvedev et al., 2017) while the second is fitting of MSTIDs direction of propagation to wind filtering mechanism (Oinats et al., 2016). Keeping in mind these two criteria, we consider our statistical results in association with the diurnal-seasonal differences in the propagation conditions of AGWs.

Daytime MSTIDs frequently appear in winter and for that season MSTID occurrence rate agrees with the hmF2 estimates of the International Reference Ionosphere (IRI-2016) model. The MSTIDs occurrence rate is higher (lower) for the MSTIDs detected at lower (higher) heights. Two diurnal minima of MSTIDs occurrence rate correspond to the two hmF2 maxima about 310 km at 04:00 UT and 330 km at 16:00 UT (Figure 4a). Thus, the MSTIDs statistics depends also on the temporal variation of the height (hmF2) from which HF radio waves were reflected. According to simulations by Vadas (2007), the dissipation rate of gravity waves increases with altitude due to increasing kinematic viscosity ( $\nu = \frac{\mu}{\rho}$ ,  $\mu$  and  $\rho$  represent the coefficient of molecular viscosity and atmospheric density, respectively). Because of this the vast majority of AGWs dissipate before reaching an altitude of 310 km.

Figure 4 shows seasonal variations of the daytime MSTIDs occurrence rate (a) and zonal wind in the vicinity of the mesopause at 80-100km (b). The low MSTID occurrence rate ( $< 0.3$ ) in summer daytime is associated with a prominent zonal wind shear. This result suggests significant impact of wind shear on the occurrence rate of MSTIDs,

which agrees with Hines and Reddy (1967) who performed model computations of the transmission coefficient of gravity wave energy for different wind and thermal conditions. They showed that horizontal winds propagating in the opposite direction to that of the gravity waves propagation can support the gravity waves energy penetration to ionospheric heights from below. However, in the case of wind shear the transmission coefficient drops to zero for all computed gravity waves periods (10, 20, 60 minutes) and wave velocities less than 100 m/s. To complement our observation with the model temperature profile at MLT region we used Naval Research Laboratory Mass Spectrometer and Incoherent Scatter radar (NRLMSISE-00) provided temperature model (shown in Figure 7). The plot depicts the NRLMSISE-00 temperature from the ground up to 500 km for seasonally representative temporal slots. The strong temperature gradient near the mesopause (indicated by an arrow in Figure 7) lead to a rapid increase of the Brunt-Väisälä frequency and a decrease of the vertical wavelength during summer, following the relation given by Equation 32 in Fritts and Alexander (2003).

$$|k_z| = \frac{N|k_h|}{\Omega} \quad (2)$$

In the above equation  $k_z$ ,  $k_h$  and stands for the vertical, and horizontal wave numbers,  $\Omega$  stands for the intrinsic frequency and  $N = \sqrt{\frac{g}{T(z)}(\frac{\partial T(z)}{\partial z} + \Gamma)}$  refers the Brunt-Väisälä frequency with  $\Gamma = \frac{g}{c_p}$  is adiabatic lapse rate. The vertical wavelength shortening enhances the wave breaking and/or dissipation rate of GW at lower thermosphere heights (Heale et al., 2020). Our results clearly show the influence of mesosphere temperature on GW propagation to higher altitudes. In Figures 4a,b, it is seen that a sharp MSTID occurrence rate decrease occurs when the mesosphere temperature becomes minimal.

Therefore, the low summer daytime MSTID occurrence rate could be explained by effects of the wind shear and sharp temperature gradient. Both reflection and dissipation prevent AGW reaching lower thermosphere heights. In the absence of a wind shear and a strong temperature gradient, the summer daytime MSTIDs would have larger occurrence rate than winter daytime MSTIDs, because the dissipation rate is less for summer daytime at heights of hmF2 ( $\sim 240$  km) than for winter daytime hmF2 ( $\sim 260$  km). The result seem in contradiction to Kozlovsky et al. (2013) work who reported MSTIDs (15 - 30 min) distribution are maximal in summer and vice versa, however they used the virtual height of reflection corresponding to selected frequency above the foE (critical frequency at E region) and below the foF2. These discrepancies might be explained by (1) in the present study we focused on longer periods portions of MSTIDs (25 - 100 min) which significantly excluded lower periodic portions; (2) in Kozlovsky et al. (2013) study their height of observation was lower F region whose lower period AGW above Brunt Väisälä period could arrive. In the present investigation those portions of MSTIDs could have been dissipated below, before reaching hmF2. On the other hand their study did not show any significant seasonal variation of long period (30 - 120 min) TIDs, which could suggest that TID signature could better be captured at maximal electron density profiles.

In a number of studies polar electrojets were proposed as main source of AGWs and MSTIDs (Francis, 1974; Samson et al., 1989; Frisell et al., 2014). However, our results do not indicate any effect of western or eastern electrojets on the generation of daytime MSTIDs. The IU and IL indices in Figures 4c and 5b, respectively, even show negative correlation with the daytime MSTIDs occurrence rate. In general, our results suggest that daytime MSTIDs are predominantly caused by the AGW generated below the mesopause rather than by auroral sources.

## 4.2 Nighttime MSTIDs

Nighttime MSTIDs are well observed in summer when the dayside MSTIDs are suppressed. To explain the dayside MSTIDs suppression we suggested that the wind shear and temperature gradient at the mesopause prevent the AGWs to penetrate above mesopause. Under such mesopause conditions, if the nightside MSTIDs are signatures of AGW they would be suppressed as well. Moreover, the nightside MSTIDs were detected at large heights above 290 km, which is not favorable for AGW-related TIDs. Nevertheless, in summer we observe a significant MSTIDs occurrence rate of  $\sim 0.4$  at night, whereas it is near zero in daytime. Hence, a mechanism other than AGWs should play the main role in the generation of nighttime MSTIDs at high latitudes. Also, the period distribution obtained from wavelet analysis shows seasonal variability of MSTID periods (see Figure 6). Winter MSTIDs are observed with wider period range than summer MSTIDs which could be due to the difference in triggering mechanism of daytime and nighttime MSTIDs.

In addition to AGW, other mechanisms have been proposed for the generation of MSTIDs, such as the auroral electrodynamics (Chimonas & Hines, 1970; Hunsucker, 1982; Kirchengast, 1997), the Perkins instability (Perkins, 1973; Hamza, 1999) and the E-F ionospheric coupling (Garcia et al., 2000; Kelley et al., 2003). MSTIDs generated due to the Perkins instability imply a certain direction of propagation and presence of a polarization electric field. Most nighttime MSTIDs observed in the northern hemisphere have wavefronts elongated from northwest to southeast, and propagate southwestward (Shiokawa, Ihara, et al., 2003; Shiokawa, Otsuka, et al., 2003; Otsuka et al., 2004) which agree with the Perkins instability. Shiokawa, Otsuka, et al. (2003) observed a polarization electric field along with the wavefronts of MSTIDs, thereby confirming that electrodynamic forces are vital for nighttime MSTIDs. Simulations by Otsuka et al. (2013) of the Perkins instability growth rate show a latitudinal dependence through the horizontal component of geomagnetic field, which is needed for the vertical component of  $\mathbf{E} \times \mathbf{B}$  plasma motion. The magnetic field inclination is large at high latitudes (it is  $77^\circ$  in Sodankylä), while significant ionization in polar summer produces a higher conductivity compared with to midlatitudes. Therefore, a high conductivity support strong ionospheric currents and polarization electric fields that can compensate for the high inclination of magnetic field. The high MSTIDs occurrence in summer nighttime is associated with the enhanced IU index that can be considered as a proxy parameter for conductivity at high latitudes (Luo et al., 2013).

However, a linear growth rate of the Perkins instability is too low to explain the experimental results (Kelley & Makela, 2001). Simulations of the electrodynamic coupling of the E and F layers show that the polarization electric fields in the E region are crucial to increase the Perkins instability growth rate in the F region (Yokoyama et al., 2009). As an evidence of the E-F coupling, S. Saito et al. (2007) showed that both quasi-periodic (QP) radar echoes from Es layers and MSTIDs are observed as horizontal banded structures extending from North-West to South-East. In summer the wind shear mechanism supports the Es layer formation (Haldoupis et al., 2007), and our results show a good agreement of the wind shear presence and summer nighttime MSTIDs occurrence rate. Therefore, E-F layer coupling could directly generate high-latitude nighttime MSTIDs or increase the Perkins instability growth rate.

The amplitude distribution (Figure 5a) allows us to consider the development of westward electrojet as a source of nighttime TIDs in winter (from September to March). The local IL index indicates auroral substorms in the vicinity of Sodankylä. The IL index increases during equinox months and decreases during summer and winter. Figure 5a,b shows that greater TID amplitudes are observed when IL index is high. A similar behaviour of TIDs amplitude and auroral electrojet (AE) index was reported for mid-latitudes by Oinats et al. (2016). Further, Francis (1974); Hunsucker (1982) pointed out that the average fluctuations of auroral electrojet in general and westward electrojet in



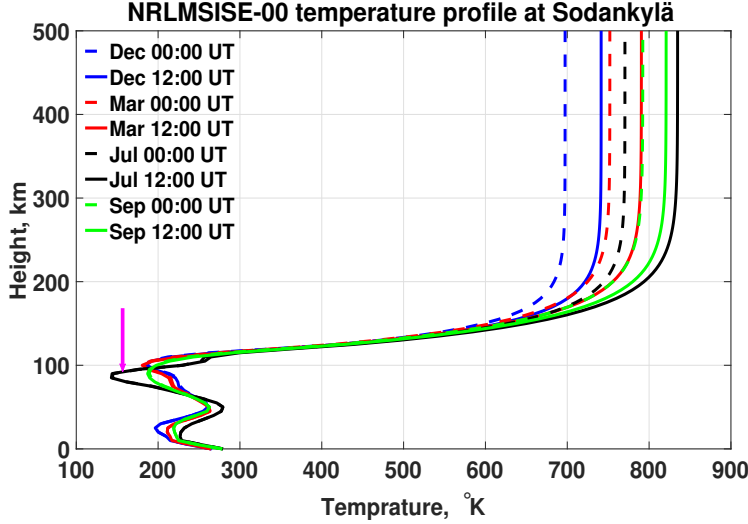


**Figure 7.** Monthly averaged NRLMSISE-00 temperature profile for seasonal representation at Sodankylä during midnight and noontime hours.

particular can be sufficient to cause AGW that can be detectable as equatorward propagating MSTIDs from high-latitudes.

On the other hand, the nighttime substorms are usually associated with particle precipitation that may cause changes in ionospheric electron density. Therefore, the higher amplitudes observed by the ionosonde could result from precipitation-induced disturbances. This may mean that the rare larger amplitudes are the consequence of nighttime particle precipitation. We also see some rare and enhanced amplitudes of TIDs after midnight in the winter months during the time of low data availability. The low data availability can be likely explained by the radio wave absorption in the D-region, which is caused by the tens-keV electron precipitation on the morning side. Kirchengast (1997) have simulated the effect of higher energy ( $> 500$  eV) electrons corresponding to the particle precipitation rooted from magnetospheric tail in inducing TIDs, and they noted that the TID induction from such thermal particle precipitation could be via inducing thermospheric heating. Consequently, those rare larger amplitudes seen in the winter nighttime hours could be random TID-like enhancements of the electron density caused by electron precipitation.

### 4.3 Dusk MSTIDs

We found that during spring and autumn a high MSTID occurrence rate was observed during dusk. These MSTIDs occur with 6-8 minutes day-to-day time drift and lifetime  $\sim 2$  hours. The observed MSTIDs occurrence rate time drift corresponds to the day-to-day change of the time of solar terminator. (Kotake et al., 2007) showed that dusk MSTIDs have wavefronts elongated from northeast to southwest and propagate northwestward. They suggest that MSTID wavefronts are almost parallel to the sunset terminator in summer. Thus, we may propose the sunset terminator as a reasonable source of dusk MSTIDs.

## 5 Conclusion

High time resolution ionosonde observations of the foF2 parameter were carried out for diurnal-seasonal statistical investigation of MSTIDs at high latitudes during the low



solar activity period of 2018-2020. We used the advantage of collocated observations of MSTIDs, mesosphere conditions and local geomagnetic activity by the ionosonde, meteor radar, and magnetometers, respectively. This gave us an opportunity to study the influence of mesosphere winds, mesosphere temperatures and polar electrojets on the statistics of MSTIDs parameters. Further, our results revealed during the daytimes, in Sodankylä (equatorward of the dayside auroral oval) mostly the midlatitude type MSTID behavior is manifested whereas during nighttimes (within the auroral oval) the high latitude MSTID characteristics were manifested. Moreover, during nighttimes a coinciding higher MSTID occurrence rate with the corresponding higher IU-index inferred conductivity despite the high magnetic inclination modulated lower Perkins instability (with respect to mid latitude) deserved Sodankylä to manifest the high latitude type MSTID.

The following major results are obtained in this study:

1. High MSTID occurrence rate of more than 0.5 prevails during daytime hours in winter months. We consider these MSTIDs as induced by AGWs. The ionosonde observations show that winter daytime MSTID occurrence rate is strongly influenced by diurnal hmF2 variations. These MSTIDs could not penetrate above 310 km heights, because of strong AGWs dissipation at these altitudes.
2. Low MSTIDs occurrence rate of less than 0.3 is observed during daytime in summer. We associate such behaviour with a strong decrease of AGWs energy transfer to ionospheric heights, due to both wind shear effect and cold mesosphere temperature conditions in summer.
3. High MSTIDs occurrence rate of more than 0.4 is observed during nighttime in summer. These MSTIDs occur in the ionosphere during unsuitable conditions for AGWs, as well as at heights above 290 km and with the presence of a wind shear in the mesosphere. We consider electrodynamic forces in the E-F region of the ionosphere as the main source of summer nighttime MSTIDs. We do not observe a direct response of MSTIDs occurrence rate to polar electrojets. However, we find seasonal correspondence of nighttime MSTIDs and the IU index as a proxy for ionospheric conductivity. Thereby, the Perkins instability and/or E-F coupling are preferred mechanisms for the summer nighttime MSTIDs generation.
4. Low data availability because of high radio wave absorption observed during nighttime in winter. In this case consideration of TID occurrence rate should be irrelevant. However, for a rare number of events we find a correspondence of TIDs amplitudes and IE index. These events seem to be classified as LSTIDs caused by geomagnetic substorms, or as ionospheric plasma irregularities caused by electron precipitation.
5. The dusk MSTIDs are predominantly observed from mid-April to mid-June and from September to mid-October with an occurrence rate up to 0.4. The sunset terminator is considered as a potential source of these MSTIDs, because they occur following the seasonal terminator appearance time.
6. For winter months the MSTID periods are shifted to longer periods and centered at 60 minutes and during summer the maximum MSTIDs periods are shorter. This also indicates that most of MSTIDs in winter and summer are caused by different mechanisms.

Overall, we performed the statistical study of MSTIDs based on a single station ionosonde observation. We cannot, however, substantiate our observation with exclusive propagation characteristics which could be addressed in the future with the aid of multiple similar high resolution sounding, in this important region.

## Data availability statement

Publically accessible Ionosonde data is found in <https://www.sgo.fi/Data/Ionosonde/ionData.php>. The electrojet indices at [https://space.fmi.fi/image/www/index.php?page=il\\_index](https://space.fmi.fi/image/www/index.php?page=il_index), IRI data at <https://kauai.ccmc.gsfc.nasa.gov/instantrun/iri/> and NRLMSISE00 data at <https://kauai.ccmc.gsfc.nasa.gov/instantrun/nrlmsis/> are available as accessed on September 29, 2023.

## Acknowledgments

This research is conducted under the Ionospheric Situational and Awareness (ISAW) project funded by Kvantum Institute at the University of Oulu. We convey our special gratitude to Sirkku Vältalo for her dedication and careful scaling of ionograms at Sodankylä Geophysical Observatory. It is worth pointing out, that Sodankylä ionosonde data are of exceptional consistency, because since 1957, all ionograms have been analysed by only three persons, and both, the second (Nina Riipi) and third (Sirkku Vältalo) scalers were students of the first scaler (Mirja Hämäläinen). AK and ML acknowledge discussions within the International Space Science Institute (ISSI) Team 23-580 “Me-teors and phenomena at the boundary between Earth’s atmosphere and outer space”.

## References

- Afraimovich, E., Boitman, O., Zhovty, E., Kalikhman, A., & Pirog, T. (1999). Dynamics and anisotropy of traveling ionospheric disturbances as deduced from transionospheric sounding data. *Radio Science*, 34(2), 477–487.
- Bristow, W., Greenwald, R., & Villain, J. (1996). On the seasonal dependence of medium-scale atmospheric gravity waves in the upper atmosphere at high latitudes. *Journal of Geophysical Research: Space Physics*, 101(A7), 15685–15699.
- Cândido, C. M. N., Pimenta, A. A., Bittencourt, J., & Becker-Guedes, F. (2008). Statistical analysis of the occurrence of medium-scale traveling ionospheric disturbances over brazilian low latitudes using oi 630.0 nm emission all-sky images. *Geophysical Research Letters*, 35(17).
- Chimonas, G., & Hines, C. (1970). Atmospheric gravity waves launched by auroral currents. *Planetary and Space Science*, 18(4), 565–582.
- Cosgrove, R. B., & Tsunoda, R. T. (2004). Instability of the e-f coupled night-time midlatitude ionosphere. *Journal of Geophysical Research: Space Physics*, 109(A4).
- Crowley, G., Ridley, A., Deist, D., Wing, S., Knipp, D., Emery, B., ... Reinisch, B. (2000). Transformation of high-latitude ionospheric f region patches into blobs during the march 21, 1990, storm. *Journal of Geophysical Research: Space Physics*, 105(A3), 5215–5230.
- Ding, F., Wan, W., Xu, G., Yu, T., Yang, G., & Wang, J.-s. (2011). Climatology of medium-scale traveling ionospheric disturbances observed by a gps network in central china. *Journal of Geophysical Research: Space Physics*, 116(A9).
- Djuth, F., Zhang, L., Livneh, D., Seker, I., Smith, S., Sulzer, M., ... Walterscheid, R. (2010). Arecibo’s thermospheric gravity waves and the case for an ocean source. *Journal of Geophysical Research: Space Physics*, 115(A8).
- Enell, C.-F., Kozlovsky, A., Turunen, T., Ulich, T., Vältalo, S., Scotto, C., & Pezzopane, M. (2016). Comparison between manual scaling and autoscala automatic scaling applied to sodankylä geophysical observatory ionograms. *Geoscientific Instrumentation, Methods and Data Systems*, 5(1), 53–64.
- Francis, S. H. (1974). A theory of medium-scale traveling ionospheric disturbances. *Journal of Geophysical Research*, 79(34), 5245–5260.
- Frissell, N., Baker, J., Ruohoniemi, J., Gerrard, A., Miller, E., Marini, J., ... Bris-

- tow, W. (2014). Climatology of medium-scale traveling ionospheric disturbances observed by the midlatitude blackstone superdarn radar. *Journal of geophysical research: space physics*, 119(9), 7679–7697.
- Fritts, D. C., & Alexander, M. J. (2003). Gravity wave dynamics and effects in the middle atmosphere. *Reviews of geophysics*, 41(1).
- Garcia, F., Kelley, M., Makela, J., & Huang, C.-S. (2000). Airglow observations of mesoscale low-velocity traveling ionospheric disturbances at midlatitudes. *Journal of Geophysical Research: Space Physics*, 105(A8), 18407–18415.
- Habarulema, J. B., Katamzi, Z. T., & McKinnell, L.-A. (2013). Estimating the propagation characteristics of large-scale traveling ionospheric disturbances using ground-based and satellite data. *Journal of Geophysical Research: Space Physics*, 118(12), 7768–7782.
- Haldoupis, C., Pancheva, D., Singer, W., Meek, C., & MacDougall, J. (2007). An explanation for the seasonal dependence of midlatitude sporadic e layers. *Journal of Geophysical Research: Space Physics*, 112(A6).
- Hamza, A. (1999). Perkins instability revisited. *Journal of Geophysical Research: Space Physics*, 104(A10), 22567–22575.
- He, K., Zhang, X., Ren, S., & Sun, J. (2016). Deep residual learning for image recognition. In *Proceedings of the ieee conference on computer vision and pattern recognition* (pp. 770–778).
- Heale, C. J., Bossert, K., Vadas, S., Hoffmann, L., Dörnbrack, A., Stober, G., ... Jacobi, C. (2020). Secondary gravity waves generated by breaking mountain waves over europe. *Journal of Geophysical Research: Atmospheres*, 125(5), e2019JD031662.
- Hines, C. O. (1960). Internal atmospheric gravity waves at ionospheric heights. *Canadian Journal of Physics*, 38(11), 1441–1481.
- Hines, C. O., & Reddy, C. (1967). On the propagation of atmospheric gravity waves through regions of wind shear. *Journal of Geophysical Research*, 72(3), 1015–1034.
- Hocke, K., Schlegel, K., et al. (1996). A review of atmospheric gravity waves and travelling ionospheric disturbances: 1982–1995. In *Annales geophysicae* (Vol. 14, p. 917).
- Hocking, W., Fuller, B., & Vandepeer, B. (2001). Real-time determination of meteor-related parameters utilizing modern digital technology. *Journal of Atmospheric and Solar-Terrestrial Physics*, 63(2-3), 155–169.
- Hunsucker, R. D. (1982). Atmospheric gravity waves generated in the high-latitude ionosphere: A review. *Reviews of Geophysics*, 20(2), 293–315.
- Jin, Y., Moen, J. I., Miloch, W. J., Clausen, L. B., & Oksavik, K. (2016). Statistical study of the gnss phase scintillation associated with two types of auroral blobs. *Journal of Geophysical Research: Space Physics*, 121(5), 4679–4697.
- Kelley, M. C., Haldoupis, C., Nicolls, M. J., Makela, J. J., Belehaki, A., Shalimov, S., & Wong, V. K. (2003). Case studies of coupling between the e and f regions during unstable sporadic-e conditions. *Journal of Geophysical Research: Space Physics*, 108(A12).
- Kelley, M. C., & Makela, J. J. (2001). Resolution of the discrepancy between experiment and theory of midlatitude f-region structures. *Geophysical Research Letters*, 28(13), 2589–2592.
- Kelley, M. C., & Miller, C. A. (1997). Electrodynamics of midlatitude spread f 3. electrohydrodynamic waves? a new look at the role of electric fields in thermospheric wave dynamics. *Journal of Geophysical Research: Space Physics*, 102(A6), 11539–11547.
- Kirchengast, G. (1997). Characteristics of high-latitude tids from different causative mechanisms deduced by theoretical modeling. *Journal of Geophysical Research: Space Physics*, 102(A3), 4597–4612.
- Kotake, N., Otsuka, Y., Ogawa, T., Tsugawa, T., & Saito, A. (2007). Statistical

- study of medium-scale traveling ionospheric disturbances observed with the  
gps networks in southern california. *Earth, planets and space*, 59(2), 95–102.
- Kozlovsky, A., Turunen, T., & Ulich, T. (2013). Rapid-run ionosonde observations  
of traveling ionospheric disturbances in the auroral ionosphere. *Journal of Geo-  
physical Research: Space Physics*, 118(8), 5265–5276.
- Krizhevsky, A., Sutskever, I., & Hinton, G. E. (2017). Imagenet classification with  
deep convolutional neural networks. *Communications of the ACM*, 60(6), 84–  
90.
- Kubota, M., Shiokawa, K., Ejiri, M., Otsuka, Y., Ogawa, T., Sakanoi, T., ... Saito,  
A. (2000). Traveling ionospheric disturbances observed in the oi 630-nm night-  
glow images over japan by using a multipoint imager network during the front  
campaign. *Geophysical research letters*, 27(24), 4037–4040.
- Lukianova, R., Kozlovsky, A., & Lester, M. (2018). Climatology and inter-annual  
variability of the polar mesospheric winds inferred from meteor radar observa-  
tions over sodankylä (67n, 26e) during solar cycle 24. *Journal of Atmospheric  
and Solar-Terrestrial Physics*, 171, 241–249.
- Luo, B., Li, X., Temerin, M., & Liu, S. (2013). Prediction of the au, al, and ae  
indices using solar wind parameters. *Journal of Geophysical Research: Space  
Physics*, 118(12), 7683–7694.
- MacDougall, J., Abdu, M. A., Batista, I., Fagundes, P., Sahai, Y., & Jayachandran,  
P. (2009). On the production of traveling ionospheric disturbances by atmo-  
spheric gravity waves. *Journal of atmospheric and solar-terrestrial physics*,  
71(17-18), 2013–2016.
- Medvedev, , Ratovsky, K., Tolstikov, M., Oinats, A., Alsatkin, S., & Zhrebtsov, G.  
(2017). Relation of internal gravity wave anisotropy with neutral wind char-  
acteristics in the upper atmosphere. *Journal of Geophysical Research: Space  
Physics*, 122(7), 7567–7580.
- Miyoshi, Y., Jin, H., Fujiwara, H., & Shinagawa, H. (2018). Numerical study of  
traveling ionospheric disturbances generated by an upward propagating gravity  
wave. *Journal of Geophysical Research: Space Physics*, 123(3), 2141–2155.
- Moges, S. T., Giday, N. M., Chekole, D. A., Ulich, T., & Sherstyukov, R. (2022).  
Storm-time observations of traveling ionospheric disturbances and ionospheric  
irregularities in east africa. *Radio Science*, 57(8), e2022RS007426.
- Nigussie, M., Moldwin, M., & Yizengaw, E. (2022). Investigating the role of gravity  
waves on equatorial ionospheric irregularities using timed/saber and c/nofs  
satellite observations. *Atmosphere*, 13(9), 1414.
- Oinats, A. V., Nishitani, N., Ponomarenko, P., Berngardt, O. I., & Ratovsky, K. G.  
(2016). Statistical characteristics of medium-scale traveling ionospheric distur-  
bances revealed from the hokkaido east and ekaterinburg hf radar data. *Earth,  
Planets and Space*, 68(1), 1–13.
- Oliver, W., Otsuka, Y., Sato, M., Takami, T., & Fukao, S. (1997). A climatology of f  
region gravity wave propagation over the middle and upper atmosphere radar.  
*Journal of Geophysical Research: Space Physics*, 102(A7), 14499–14512.
- Oluwadare, T. S., Jakowski, N., Valladares, C. E., Akala, A. O.-O., Abe, O. E., Al-  
izadeh, M. M., & Schuh, H. (2022). Climatology of medium-scale traveling  
ionospheric disturbances (mstids) observed with gps networks in the north  
african region. *Pure and Applied Geophysics*, 1–22.
- Otsuka, Y. (2021). Medium-scale traveling ionospheric disturbances. *Ionosphere Dy-  
namics and Applications*, 421–437.
- Otsuka, Y., Shiokawa, K., Ogawa, T., & Wilkinson, P. (2004). Geomagnetic conju-  
gate observations of medium-scale traveling ionospheric disturbances at midlat-  
itude using all-sky airglow imagers. *Geophysical research letters*, 31(15).
- Otsuka, Y., Suzuki, K., Nakagawa, S., Nishioka, M., Shiokawa, K., & Tsugawa, a.  
(2013). Gps observations of medium-scale traveling ionospheric disturbances  
over europe. In *Annales geophysicae* (Vol. 31, pp. 163–172).

- Perkins, F. (1973). Spread f and ionospheric currents. *Journal of Geophysical Research*, 78(1), 218–226.
- Pimenta, A. A., Kelley, M., Sahai, Y., Bittencourt, J. A., & Fagundes, P. (2008). Thermospheric dark band structures observed in all-sky of 630 nm emission images over the Brazilian low-latitude sector. *Journal of Geophysical Research: Space Physics*, 113(A1).
- Saito, A., Nishimura, M., Yamamoto, M., Fukao, S., Tsugawa, T., Otsuka, Y., & Miyazaki, S. (2002). Observations of traveling ionospheric disturbances and 3-m scale irregularities in the nighttime f-region ionosphere with the MU radar and a GPS network. *Earth, planets and space*, 54(1), 31–44.
- Saito, S., Yamamoto, M., Hashiguchi, H., Maegawa, A., & Saito, A. (2007). Observational evidence of coupling between quasi-periodic echoes and medium scale traveling ionospheric disturbances. In *Annales geophysicae* (Vol. 25, pp. 2185–2194).
- Samson, J., Greenwald, R., Ruohoniemi, J., & Baker, K. (1989). High-frequency radar observations of atmospheric gravity waves in the high-latitude ionosphere. *Geophysical research letters*, 16(8), 875–878.
- Sherstyukov, R., Akchurin, A., & Sherstyukov, O. (2018). Collocated ionosonde and dense GPS/GLONASS network measurements of midlatitude MSTIDs. *Advances in Space Research*, 61(7), 1717–1725.
- Shiokawa, K., Ihara, C., Otsuka, Y., & Ogawa, T. (2003). Statistical study of nighttime medium-scale traveling ionospheric disturbances using midlatitude airglow images. *Journal of Geophysical Research: Space Physics*, 108(A1).
- Shiokawa, K., Mori, M., Otsuka, Y., Oyama, S., Nozawa, S., Suzuki, S., & Connors, M. (2013). Observation of nighttime medium-scale travelling ionospheric disturbances by two 630-nm airglow imagers near the auroral zone. *Journal of Atmospheric and Solar-Terrestrial Physics*, 103, 184–194.
- Shiokawa, K., Otsuka, Y., Ihara, C., Ogawa, T., & Rich, F. (2003). Ground and satellite observations of nighttime medium-scale traveling ionospheric disturbance at midlatitude. *Journal of Geophysical Research: Space Physics*, 108(A4).
- Simonyan, K., & Zisserman, A. (2014). Very deep convolutional networks for large-scale image recognition. *arXiv preprint arXiv:1409.1556*.
- Szegedy, C., Vanhoucke, V., Ioffe, S., Shlens, J., & Wojna, Z. (2016). Rethinking the inception architecture for computer vision. In *Proceedings of the IEEE conference on computer vision and pattern recognition* (pp. 2818–2826).
- Tanskanen, E. (2009). A comprehensive high-throughput analysis of substorms observed by image magnetometer network: Years 1993–2003 examined. *Journal of Geophysical Research: Space Physics*, 114(A5).
- Torrence, C., & Compo, G. P. (1998). A practical guide to wavelet analysis. *Bulletin of the American Meteorological Society*, 79(1), 61–78.
- Tsugawa, T., Otsuka, Y., Coster, A., & Saito, A. (2007). Medium-scale traveling ionospheric disturbances detected with dense and wide TEC maps over North America. *Geophysical Research Letters*, 34(22).
- Tsunoda, R. T. (2008). A digest of electrodynamic coupling and layer instabilities in the nighttime midlatitude ionosphere. *Geophysical Monograph Series*, 181, 283–290.
- Vadas, S. L. (2007). Horizontal and vertical propagation and dissipation of gravity waves in the thermosphere from lower atmospheric and thermospheric sources. *Journal of Geophysical Research: Space Physics*, 112(A6).
- Xu, J., Liu, H.-L., Yuan, W., Smith, A., Roble, R., Mertens, C., ... Mlynarczyk, M. (2007). Mesopause structure from thermosphere, ionosphere, mesosphere, energetics, and dynamics (timed)/sounding of the atmosphere using broadband emission radiometry (saber) observations. *Journal of Geophysical Research: Atmospheres*, 112(D9).

771 Yokoyama, T., Hysell, D. L., Otsuka, Y., & Yamamoto, M. (2009). Three-  
772 dimensional simulation of the coupled perkins and es-layer instabilities in  
773 the nighttime midlatitude ionosphere. *Journal of Geophysical Research: Space*  
774 *Physics*, 114(A3).